Imprints of the Janis-Newman-Winicour spacetime on observations related to shadow and accretion

Subhadip Sau,[*] Indrani Banerjee,[†] and Soumitra SenGupta[‡]
School of Physical Sciences, Indian Association for the Cultivation of Science,
2A & 2B Raja S. C. Mullick Road, Kolkata-700032, India

(Received 9 April 2020; revised 18 June 2020; accepted 24 August 2020; published 9 September 2020)

The final fate of gravitational collapse of massive stars has been a subject of interest for a long time since such a collapse may lead to black holes and naked singularities alike. Since, the formation of naked singularities is forbidden by the cosmic censorship conjecture, exploring their observational differences from black holes may be a possible avenue to search for these exotic objects. The simplest possible naked singularity spacetime emerges from the Einstein massless scalar field theory with the advantage that it smoothly translates to the Schwarzschild solution by the variation of the scalar charge. This background, known as the Janis-Newman-Winicour spacetime is the subject of interest in this work. We explore electromagnetic observations around this metric which involves investigating the characteristics of black hole accretion and shadow. We compute the shadow radius in this spacetime and compare it with the image of M87*, recently released by the Event Horizon Telescope Collaboration. Similarly, we derive the expression for the luminosity from the accretion disk and compare it with the observed optical luminosity of eleven Palomar Green quasars. Our analysis indicates that the shadow of M87* and the quasar optical data consistently favor the Schwarzschild background over the Janis-Newman-Winicour spacetime. The implications of this result are discussed.

DOI: 10.1103/PhysRevD.102.064027

I. INTRODUCTION

One of the classic unresolved problems in general relativity is the ultimate fate of the gravitational collapse of a massive body, such as a star. It has been conjectured that the end state of any generic complete gravitational collapse leads to a Kerr black hole characterized by only its mass and angular momentum. All other information regarding the initial conditions of the collapse, the symmetries and the nature of matter fields that were present in the beginning of the collapse gets radiated away. It turns out that it is very difficult to prove this conjecture either analytically or numerically and therefore one cannot definitively say that the ultimate fate of a gravitational collapse always leads to the formation of a black hole. In fact, investigations reveal that such gravitational collapse with a set of allowed initial conditions often lead to the formation of naked singularities [1–11], even though such objects are forbidden by the cosmic censorship conjecture [12].

While the end products of gravitational collapse continue to be debatable, it is worth exploring the observational differences between black holes and naked singularities, assuming that they have been formed by some mechanism. Given the surfeit of data available in the electromagnetic domain, this has intrigued researchers worldwide since such a study can enhance our understanding regarding the nature of compact objects at the galactic centers or in the x-ray binaries. Observations related to accretion disks [13–19] or gravitational lensing [20–26] have revealed that black holes and naked singularities often exhibit strikingly different properties which can be used as a possible probe to differentiate between them. Further, ultra high energy collisions and fluxes of the escaping collision products can be another possible tool to discern between the two different entities [27]. There are however cases when certain wormhole spacetimes and naked singularities exhibit similar observational features like that of a black hole which makes the differentiation quite difficult [28–31]. However, this will be kept outside the purview of the present discussion.

In the present work we consider the Janis-Newman-Winicour (JNW) naked singularity which represents an exact solution of the Einstein's equations with a massless scalar field [32]. This solution was originally derived by Fisher [33] in a different parametrization while Bronnikov and Khodunov [34] subsequently studied its stability. It was later rediscovered by Wyman [35] and the equivalence of the Wyman solution with the Janis-Newman-Winicour spacetime was established by Virbhadra [36]. It is interesting to note that addition of the massless scalar field in the action changes the nature of the spherically symmetric and

---

[*] tpss2@iacs.res.in
[†] tpib@iacs.res.in
[‡] tpssg@iacs.res.in

asymptotically flat exact metric solution from the Schwarzschild black hole to the JNW naked singularity. Consequently, it can be shown that one can recover the Schwarzschild metric from the JNW spacetime by continuously adjusting a single metric parameter representative of the scalar charge of the naked singularity.

There exists several works in the literature which explored the optical properties of the Janis-Newman-Winicour spacetime, e.g., gravitational lensing and relativistic images [23–26,37], accretion and shadow [21,22,37,38]. The aim of this work is to explore the nature of shadow and the emission from the accretion disk around the Janis-Newman-Winicour spacetime and compare them with the available observations. The optical luminosity of eighty Palomar Green quasars and the recently released shadow of M87* are used as the observational sample for comparing the theoretical results.

The paper is organized as follows: In Sec. II we review the basic properties of the Janis-Newman-Winicour spacetime. We study the structure of the shadow cast by the JNW spacetime and compare it with the image of M87* in Sec. III. Section IV serves as a quick overview over the "thin accretion disk" model proposed by Novikov and Thorne which helps us to evaluate the accretion disk luminosity for a sample of eighty Palomar Green quasars. Subsequently we compare this with the observed luminosity of the quasars to distinguish the JNW spacetime from the Schwarzschild background. We end with a summary of our results and the concluding remarks in Sec. V.

We use (-,+,+,+) as the metric convention and will work with geometrized units taking $G = c = 1$.

II. JANIS-NEWMAN-WINICOUR SPACETIME: A QUICK REVIEW

In this work we consider the Einstein massless scalar (EMS) field theory such that the massless scalar field is minimally coupled to gravity. The associated action is given by

$$S = \int d^4x\sqrt{-g}\left[\frac{R}{2\kappa^2} - \frac{1}{2}\partial_\mu\phi(r)\partial^\mu\phi(r)\right] \tag{1}$$

where, g and R are respectively, determinant of the metric tensor and the Ricci scalar, $\kappa^2 = 8\pi G$ (G is the four-dimensional gravitational constant) and $\phi(r)$ is the minimally coupled scalar field. In four dimension, the corresponding Einstein's gravitational field equations derived from the above action has an exact static and spherically symmetric solution [36,39,40] given by,

$$ds^2 = -\left(1-\frac{b}{r}\right)^{\gamma}dt^2 + \left(1-\frac{b}{r}\right)^{-\gamma}dr^2 + \left(1-\frac{b}{r}\right)^{1-\gamma}r^2(d\theta^2 + \sin^2\theta d\phi^2) \tag{2}$$

which is popularly known as the Janis-Newman-Winicour (JNW) solution in the literature. In Eq. (2) r represents the radial coordinate, $0 \leq \gamma \leq 1$ and $b\gamma = 2M$, such that the Schwarzschild metric is retrieved when $\gamma = 1$. There is a curvature singularity at $r = b$ which is also the location of the event horizon. Since the singularity is not cloaked by the event horizon this metric represents a naked singularity and hence we confine ourselves in the region $r > b$. The solution for the scalar field and the associated energy-momentum tensor are respectively given by

$$\phi(r) = \frac{q}{b}\ln\left(1-\frac{b}{r}\right) \quad \text{and} \tag{3}$$

$$T_{\mu\nu} = \partial_\mu\phi\partial_\nu\phi - \frac{1}{2}g_{\mu\nu}\partial^\alpha\phi\partial_\alpha\phi \tag{4}$$

where b is related to the scalar charge q by,

$$b = 2\sqrt{M^2 + q^2} \tag{5}$$

such that smaller γ corresponds to a larger magnitude of the scalar field.

In the context of string theory a pseudoscalar field known as the axion, arises as the dual of the field strength of the Kalb-Ramond field $B_{\mu\nu}$ minimally coupled to Einstein gravity in four dimensions. The Kalb-Ramond field $B_{\mu\nu}$ with the transformation property of a second rank antisymmetric tensor gauge field has the following action,

$$S_{KR} = \int d^4x\sqrt{-g}\left[\frac{R}{2\kappa^2} - \frac{1}{12}H_{\mu\nu\alpha}H^{\mu\nu\alpha}\right] \tag{6}$$

where $H_{\alpha\mu\nu} = \partial_{[\alpha}B_{\mu\nu]}$ is the field strength tensor which has the pseudoscalar axion field H as its dual,

$$H^{\alpha\mu\nu} = \epsilon^{\alpha\mu\nu\beta}\partial_\beta H \tag{7}$$

In terms of the axion field the energy-momentum tensor of the Kalb-Ramond field can be written as

$$T_{\mu\nu} = \partial_\mu H\partial_\nu H - \frac{1}{2}g_{\mu\nu}\partial^\sigma H\partial_\sigma H \tag{8}$$

which resembles Eq. (4).

Under a different choice of the metric ansatz, the resultant static, spherically symmetric and asymptotically flat solution of the Einstein's equations (associated with the Kalb-Ramond field) assumes a perturbative solution of the form [41],

$$ds^2 = -e^{\nu(r)}dt^2 + e^{\lambda(r)}dr^2 + r^2d\Omega^2 \tag{9}$$

such that

$$e^{\nu(r)} = 1 - \frac{2M}{r} + \frac{hM}{r^3} + \mathcal{O}\left(\frac{1}{r^4}\right) \tag{10a}$$

$$e^{-\lambda(r)} = 1 - \frac{2M}{r} + \frac{3h}{r^2} + \mathcal{O}\left(\frac{1}{r^4}\right) \tag{10b}$$

where h refers to the axion parameter and has dimensions of M^2. For the solution of the Kalb-Ramond field strength and the axion field one is referred to [41]. Just like the JNW space time this metric also smoothly translates to the Schwarzschild solution in the event the axion parameter h vanishes.

We have already explored the properties of accretion and shadow in the spacetime with the axionic charge [42,43]. Observational implications of several other alternative gravity models have been extensively studied in the literature [44–51]. In this work, we will explore the motion of both the massless and the massive particles around the Janis-Newman-Winicour (JNW) spacetime. In the case of massive particles we will study accretion of matter, while the properties of the black hole shadow can be investigated by studying motion of the massless particles. In both cases we will confront our theoretical findings with the available observations to provide constrain on the metric parameter γ. In each case we will compare our findings with the results obtained previously for the axion metric [Eq. (9), Eq. (10a), Eq. (10b)].

III. SHADOW CAST BY THE COMPACT OBJECT GOVERNED BY THE JANIS-NEWMAN-WINICOUR SPACETIME

With the advent of the Event Horizon Telescope, it has been possible to obtain the image of the central compact object in the galaxy M87. This has enabled direct observations of the near horizon regime of a black hole and has opened up a new and independent window to test the nature of strong gravity. The shadow refers to the gravitationally lensed projection of the photon circular orbits onto the observer's sky. When light from a distant source or the surrounding accretion disk come close to the photon sphere, a part of it falls into the compact object while the remaining escapes to infinity [52–56]. Consequently, the observer perceives a dark patch in the local sky known as the shadow. The boundary of the shadow testifies strong gravitational lensing near the photon sphere and hence the shape and size of the shadow captures useful information regarding the nature of the background spacetime [20,54,57–61]. In what follows, we will study the nature of the shadow cast by the JNW spacetime and confront it with the observed shadow of M87*. We initiate by first exploring the structure of the shadow in a most general spherically symmetric spacetime.

A. Structure of the shadow in a general spherically symmetric background

In this section, we work out the structure of the black hole shadow in a general static and spherically symmetric background given by

$$ds^2 = -e^{\nu(r)}dt^2 + e^{\lambda(r)}dr^2 + \mathcal{R}^2(r)r^2(d\theta^2 + \sin^2\theta d\phi^2). \tag{11}$$

This metric ansatz is a more generalized form than the one usually used in the literature due to its modified volume factor, i.e., the coefficient of $d\Omega^2$ is not just r^2 but also has a function of r multiplied to it. This is important since we are eventually interested in studying the properties of the shadow in a metric given by Eq. (2).

Due to the time and zenithal angle independence of the metric, the energy E and the total angular momentum L of the photons are conserved. The constants of motion are given by,

$$E = -g_{tt}u^t = -p_t \quad \text{and} \tag{12a}$$

$$L = g_{\phi\phi}u^\phi = p_\phi \tag{12b}$$

respectively. The Hamilton-Jacobi equation can therefore be integrated to obtain the following solution for the action,

$$S = -Et + L\phi + \bar{S}(r,\theta) \tag{13}$$

where $\bar{S}(r,\theta)$ is an arbitrary function of radial and angular coordinates. Assuming separability of $\bar{S}(r,\theta)$ as $\bar{S}(r,\theta) = S^r(r) + S^\theta(\theta)$, and substituting the Hamilton-Jacobi equation for r and θ in the Hamiltonian we obtain,

$$\mathcal{R}^2r^2\left(k + e^{-\nu(r)}E^2 - e^{-\lambda(r)}\left(\frac{dS^r}{dr}\right)^2\right) = \left(\frac{dS^\theta}{d\theta}\right)^2 + \frac{L^2}{\sin^2\theta} = C + L^2 \tag{14}$$

where the separation constant C, known as the Carter constant represents a third constant of motion [62]. Therefore the geodesic equations for r and θ are given by,

$$e^{\lambda+\nu}\dot{r}^2 = -e^\nu\frac{C+L^2}{r^2\mathcal{R}^2} + E^2 \equiv -V_{\rm eff}(r) + E^2 \equiv \mathbf{R}(r) \quad \text{and} \tag{15}$$

$$(\mathcal{R}^2r^2\dot{\theta})^2 = C - L^2\cot^2\theta \equiv E^2\Theta(\theta) \tag{16}$$

respectively, where

$$V_{\rm eff} = e^\nu\frac{C+L^2}{r^2\mathcal{R}^2} \tag{17}$$

represents the effective potential for radial motion of photon, while

$$\Theta(\theta) = \chi - l^2 \cot^2 \theta \tag{18}$$

such that $\chi = C/E^2$ and $l = L/E$. The radius of the photon sphere r_{ph} is defined such that the radial velocity $\dot{r}$ vanishes and the effective potential $V_{\rm eff}(r)$ possesses an extrema. Generally this turns out to be a maxima, representing an unstable equilibrium of the photon, resulting in either fall into the gravitating object or escaping to infinity due to even slight perturbation. Consequently, photon sphere plays the important role in determining the boundary of the shadow.

Therefore, r_{ph} is obtained by solving $\mathbf{R}(r) = \mathbf{R}'(r) = V'_{\rm eff}(r) = 0$, such that the above conditions yield

$$\chi + l^2 = \mathcal{R}^2(r_{ph}) r_{ph}^2 e^{-\nu(r_{ph})} \quad \text{and} \tag{19}$$

$$\nu'(r_{ph}) = 2\left[\frac{1}{r_{ph}} + \frac{\mathcal{R}'(r_{ph})}{\mathcal{R}(r_{ph})}\right] \tag{20}$$

respectively. The photon sphere in an arbitrary spherically symmetric metric is therefore obtained by solving Eq. (20) for r. In the limit $\mathcal{R} = 1$ we get back the known result $r\nu' = 2$ [43].

The contour of the black hole shadow in the observer's sky is obtained by considering the projection of the photon sphere in the image plane [63]. Determination of the shadow outline depends on the largest positive radius obtained by solving Eq. (20) [52,53]. Two celestial coordinates α and β which are directly related to l and χ designates the locus of the shadow boundary [53,63].

Following the prescription as given in [43,53], it can be shown that

$$\alpha^2 + \beta^2 = \chi + l^2 = r_{sh}^2. \tag{21}$$

From the above analysis it can be concluded that for any general static, spherically symmetric and asymptotically flat metric the shadow is circular in shape and depends on the radius of photon sphere which in turn solely depends only on the g_{tt} component of the metric. We also note that for an asymptotically flat observer the radius of the shadow does not depend on the distance r_0 and the inclination angle θ_0 of the observer.

B. Shadow of the compact object governed by the Janis-Newman-Winicour spacetime

In this section we will study the properties of the shadow given by the metric in Eq. (2). Before we proceed with the discussion of the shadow, we first plot the effective potential discussed in the last section in Fig. 1(a). The figure depicts the behavior of the effective potential with the variation of the metric parameter γ. As expected, the effective potential $V_{\rm eff}$ has a maxima occurring at the photon sphere r_{ph}, which depends on the value of γ. On decreasing the scalar charge q (or increasing γ), r_{ph} becomes smaller along with the height of the potential.

We can further determine the radius of the photon sphere and the shadow using Eq. (20) and Eq. (21) for the metric in Eq. (2). These are given by

$$r_{ph} = b\left(\gamma + \frac{1}{2}\right) \quad \text{and} \tag{22}$$

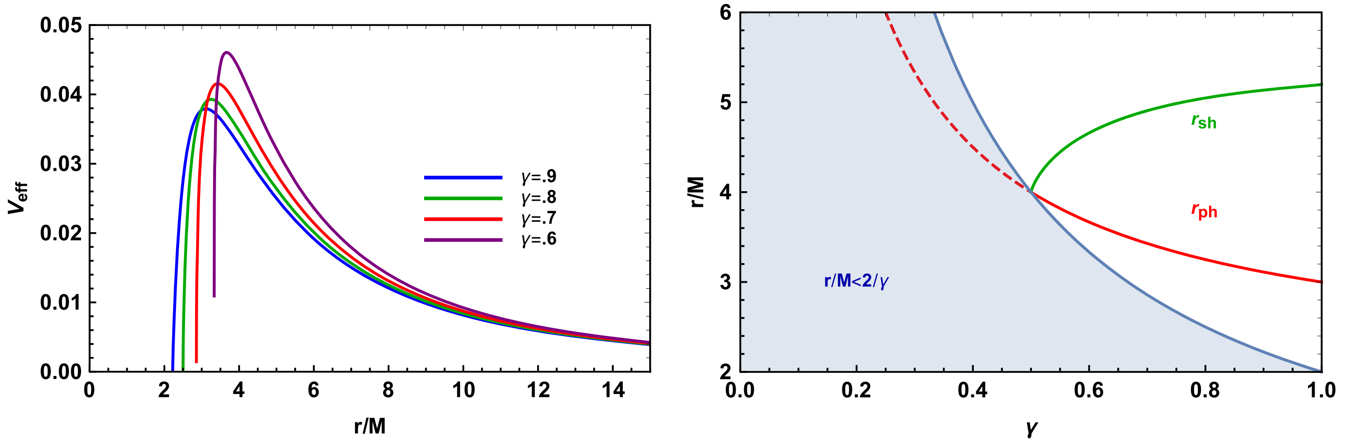

(a) (b)

FIG. 1. The above figure depicts the dependence of (a) the effective potential (b) the photon sphere r_{ph} and the radius of the shadow r_{sh} on the metric parameter γ. The metric has a curvature singularity at $r_c = b$ where $b = 2M/\gamma$. The region of unphysical solutions $(r < b)$ is shaded in blue. We note that at $\gamma = 0.5$ both $r_{ph} = r_{sh} = r_c = b$. When $\gamma < 0.5$, the photon sphere disappears since $r_{ph} < r_c$. We therefore confine ourselves in the region $r > r_c$ and $0.5 \leq \gamma \leq 1$.

$$r_{sh} = b\left(\gamma + \frac{1}{2}\right)\left(\frac{2\gamma - 1}{2\gamma + 1}\right)^{\frac{1}{2}-\gamma} \tag{23}$$

respectively. In Eq. (22) and Eq. (23) the r_{ph} and r_{sh} are expressed in units of M. In what follows we will scale the radial coordinate by the mass M of the black hole, such that $r \equiv r/M$. Consequently, $b \equiv b/M$, the scalar charge $q \equiv q/M$ and the axion parameter $h \equiv h/M^2$. From Sec. II we recall that $b\gamma = 2$ and $0 \leq \gamma \leq 1$. We note that as we decrease the value of γ from unity, the radius of the photon sphere r_{ph} increases while that of the shadow r_{sh} decreases. At $\gamma = 0.5$ both r_{ph} and r_{sh} become equal to $r_c = b$, the radius where the curvature singularity occurs. When $\gamma < 0.5$, $r_{ph} < r_c$ and therefore we confine ourselves in the region $0.5 \leq \gamma \leq 1$. The above discussion is illustrated in Fig. 1(b). The region of unphysical solutions ($r < b$) is shaded in blue. As soon as the field parameter γ approaches the critical value $\gamma = 0.5$, physical solutions for r_{ph} and r_{sh} ceases to exist.

At a glance, this atypical behavior of photon sphere and shadow seems counterintuitive since the radius of the shadow generally increases with the radius of the photon sphere. In this respect the behavior of the Winicour solution is quite unique. But one can understand this scenario with the analogy of having an optical lens system in a medium denser than air. Optical system in relatively denser medium bends light relatively smaller. Similarly, increasing the scalar charge q is equivalent to putting the optical system in a relatively denser medium, i.e., a medium with larger refractive index. Consequently, light bending is maximum in the Schwarzschild scenario compared to the situation where there is scalar charge. The diagrammatic realization has been shown in Fig. 2 which clearly shows that the presence of scalar field causes lesser deflection of light compared to the Schwarzschild scenario.

Finally we end our discussion with a few interesting comments:

(i) We have noted from Sec. II that the scalar field and the Kalb-Ramond field both minimally coupled to gravity give rise to identical energy-momentum tensor. However, in the case of the scalar field the solution of the gravitational field equations lead to an exact metric representing a naked singularity while in the other case the solution leads to a perturbative metric representing a black hole. We have explored in an earlier work [43] the dependence of the shadow radius on the axion parameter h and found that a negative h enhances, while a positive h diminishes the shadow compared to the Schwarzschild scenario Fig. 3(a). In the Winicour solution on the other hand, the shadow decreases with decrease in γ (or increase with the scalar charge q) and its radius is always less than the Schwarzschild case. This is illustrated in Fig. 3(b).

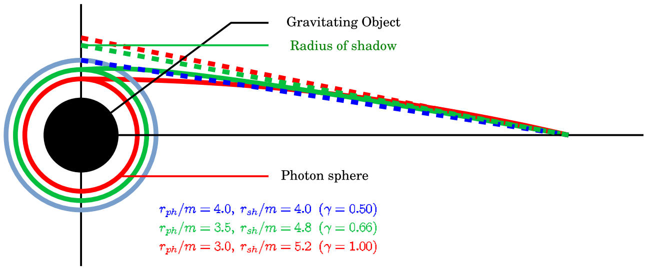

FIG. 2. Diagrammatic realisation of gravitational lensing in Winicour spacetime.

(ii) We note from Fig. 3(b) that the Schwarzschild scenario produces larger radius of the shadow compared to the ones with nontrivial scalar charge. Further, if we allow the black hole to be rotating in general relativity (the Kerr black hole), the radius of the shadow also turns out to be smaller than the Schwarzschild scenario. It is therefore interesting to understand if a Kerr black hole can be distinguished from the ones with scalar charge from shadow related observations.

In this context it is important to note that the spin a of the black hole not only affects the size of the shadow but also its shape. This becomes pronounced at a high inclination angle as the presence of angular momentum leads to a dented shadow thereby causing a deviation from circularity in its shape. At low inclination angles this effect is less conspicuous. In particular, it can be shown that if a black hole is viewed face on (zero inclination angle) then the shadow is circular although the radius of the shadow depends on the black hole angular momentum. To elucidate this point we note that the x and y coordinates of the shadow for a Kerr black hole are given by,

$$x = -\frac{l}{\sin i} \quad y = \pm\sqrt{\chi + a^2\cos^2 i - l^2\cot^2 i}. \tag{24}$$

In Eq. (24), i refers to the inclination angle, a is the dimensionless black hole spin parameter, $l = L/E$ and $\chi = C/E^2$ are the two impact parameters, such that L is the specific angular momentum, E is the specific energy and C refers to the Carter constant. The derivation of Eq. (24) can be found in [52,53]. From Eq. (24) it can be shown that when $i = 0$ the contour of the shadow is given by,

$$x^2 + y^2 = \chi + a^2 = r_{sh}^2 \quad \text{where} \tag{25}$$

$$\chi = -\frac{r_{ph}^3(r_{ph}^3 + 9r_{ph} - 6r_{ph}^2 - 4a^2)}{a^2(r_{ph} - 1)^2} \tag{26}$$

depends on a and r_{ph} [52,53,64]. The radius of the photon sphere r_{ph} in turn also depends on a and is given by,

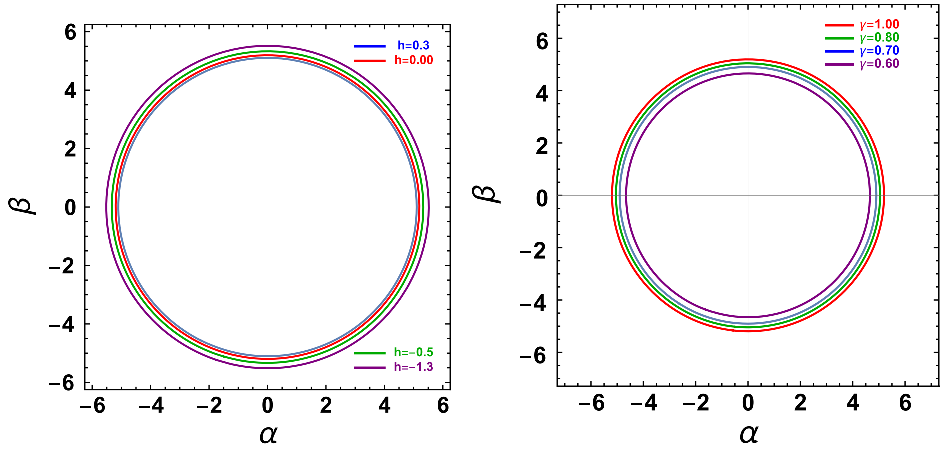

(a) (b)

FIG. 3. Radius of the shadow for (a) the perturbative axion metric and (b) the exact Winicour solution for various values of their respective metric parameters.

$$\begin{cases} r_{ph} = 1 + \sqrt{A}\left[\left\{B + \sqrt{B^2+1}\right\}^{\frac{1}{3}} + \left\{B + \sqrt{B^2+1}\right\}^{-\frac{1}{3}}\right] & \text{if } |B| > 1 \\ r_{ph} = 1 + 2\sqrt{A}\cos(\frac{1}{3}\cos^{-1}B) & \text{if } \; |B| \leq 1 \end{cases} \tag{27}$$

where

$$A = \frac{3 - a^2}{3} \quad B = \frac{1 - a^2}{A^{\frac{3}{2}}}. \tag{28}$$

Figure 4 depicts the variation of the shadow radius with the Kerr parameter a (considering $i = 0$) and the JNW metric parameter γ. It is clear from Fig. 4(a) that for $i = 0$ an increase in Kerr parameter decreases the shadow radius. Similarly, if we have a spherically symmetric black hole with scalar charge described by the JNW spacetime, the radius of the shadow diminishes with an increase in scalar charge q (or decrease in γ). However, the degree of reduction in the shadow radius is more due to the presence of scalar charge than when it is rotating ($r_{sh} \sim 4.0R_g$ when $\gamma = 0.5$ while $r_{sh} \sim 4.83R_g$ when $|a| \sim 1$ compared to $r_{sh} \sim 5.196R_g$ in the Schwarzschild scenario). This directly affects the angular diameter θ of the shadow, since

$$\tan\theta \approx \theta = \frac{2r_{sh}GM}{Dc^2} \tag{29}$$

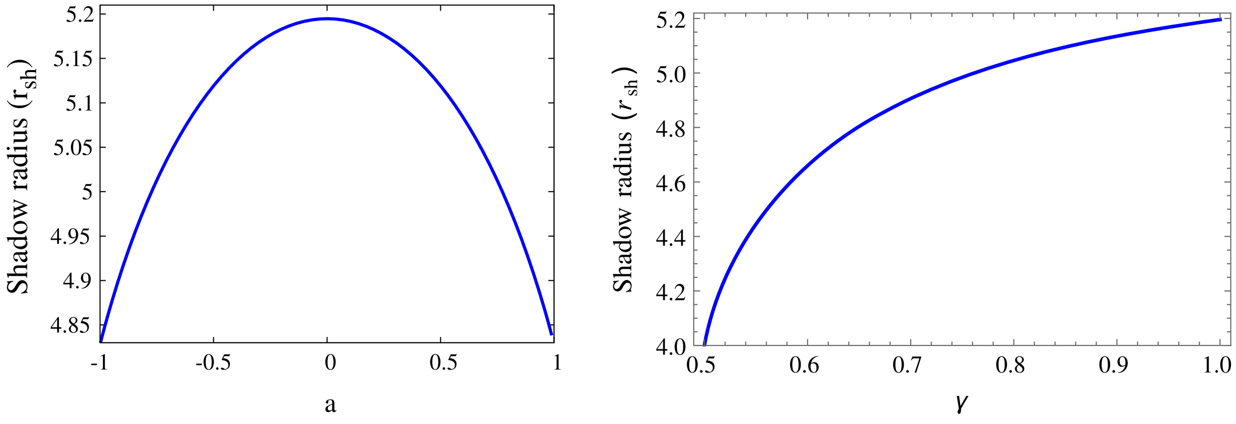

(a) (b)

FIG. 4. The figure illustrates the variation of the shadow radius with (a) the Kerr parameter a (the black hole viewed at $i = 0$) and (b) the metric parameter γ of the Janis Newman Winicour spacetime.

such that M is the mass and D is the distance of the black hole from the observer. This result has important implications with respect to the observed shadow of M87* which we shall discuss in the next section.

(iii) We could have considered the metric ansatz in Eq. (2) by removing the constraint $b\gamma = 2M$ and kept γ and b independent. Such a metric ansatz is compatible with the Einstein's equations with the minimally coupled scalar field. We refer to such a metric as the generalized Janis-Newman-Winicour solution. The interesting characteristic of this generalized solution is that we do not get physical solutions for the photon sphere and the shadow for all values of the metric parameters γ and b.

In Fig. 5, the regions $b > 0$, $\gamma < 0$ and $b < 0$, $\gamma > 0.5$, produces negative radii for the photon sphere and the shadow and hence are not physically important. As discussed in Sec. III B real positive solution of the shadow is achievable only if $|\gamma| > 0.5$. In fact for the region $|\gamma| < 0.5$, no physically realizable solution of photon sphere and shadow can be found [Fig. 1(b)]. Hence the observation of shadow may be possible if $b > 0$, $\gamma > 1/2$ or $b < 0$, $\gamma < -1/2$. The second scenario where b and γ are negative is not much discussed in the literature. However when we are in the region $b > 0$ we must have $\gamma b = 2$, so that we can reproduce the Schwarzschild limit for the gravitating object. This particular case when $b > 0$ is widely known as Janis-Newman-Winicour solution. Hence in this region, our two parameter solution reduces to one parameter solution discussed earlier. For the particular case when $\gamma = 1$, the solution in Eq. (2) represents the Schwarzschild solution.

C. Comparison with the observed shadow of M87*

We have noted in the last section that a Kerr black hole casts a noncircular shadow only if it is viewed at a high inclination angle. On the other hand, if a black hole casts a circular shadow despite being viewed at high inclination angle, then it implies that the background spacetime is spherically symmetric. Further, if the black hole has precise and independent measurements of mass and distance, then the size of the observed angular diameter can be used to compare between various background spacetimes. Since the angular diameter directly depends on the shadow radius [Eq. (29)], an observed angular diameter smaller than the Schwarzschild scenario might favor the JNW spacetime. Therefore in a future observation, if a black hole is viewed at high inclination angle and has precise and independent measurements of its mass and distance, then the shape and size of the shadow can be a useful tool to probe the background spacetime. In this way the degeneracy between the effect of spin and γ can be broken, although we need to wait for future observations for this.

At present, only the angular diameter of M87*, the supermassive black hole at the center of the galaxy M87, has been measured which corresponds to $42 \pm 3\ \mu as$. The object exhibits a strong jet and the angle of inclination is taken to be 17° which the jet axis makes to the line of sight. This is in agreement with the nearly circular shadow observed in M87* with deviation from circularity $\Delta C \leq 10\%$ [65]. Based on stellar population measurements, the distance of M87* is reported to be $D = (16.8 \pm 0.8)$ Mpc [66–68]. The mass of the source is constrained to be $M \sim 6.2^{+1.1}_{-0.5} \times 10^9\ M_\odot$ [69] from stellar dynamics observations while $M \sim 3.5^{+0.9}_{-0.3} \times 10^9\ M_\odot$ [70] from gas dynamics studies. Note that these are independent mass

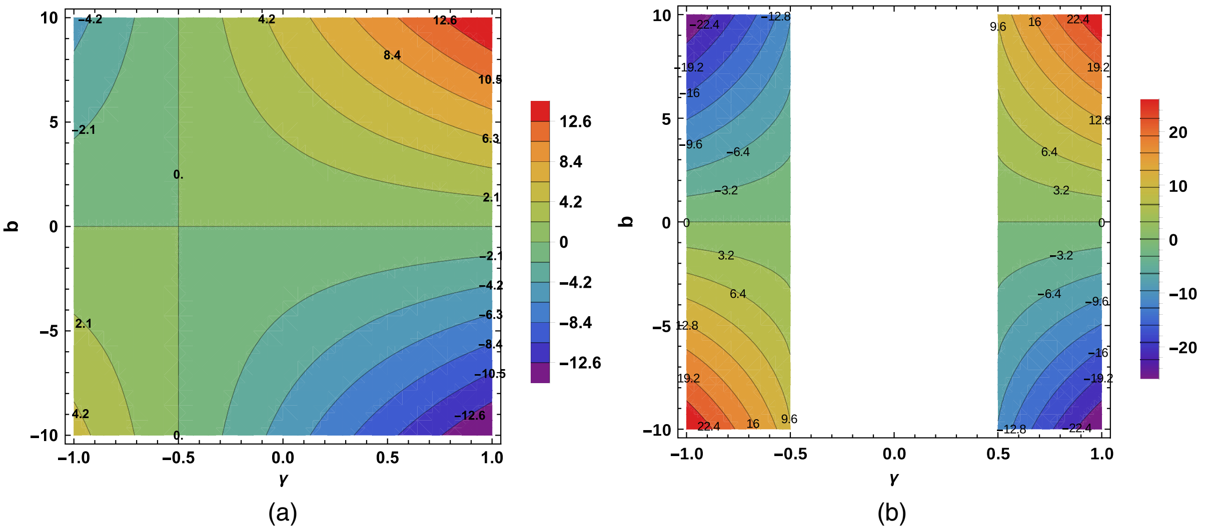

FIG. 5. The above figure represents the constant contours of the radius of the (a) photon sphere and (b) the shadow as functions of the metric parameters γ and b. The shadow and the photon sphere are expressed in units of GM/c^2.

TABLE I. Variation of angular diameter of M87* with Kerr parameter a, JNW metric parameter γ and black hole mass M. The distance of the source is assumed to be $D = 16.8$ Mpc while computing the angular diameter.

		Angular diameter (in μas)					
		Kerr metric ($i = 0$)			JNW metric		
Serial No.	Mass (In units of $10^9\ M_\odot$)	$a = 1.0$	$a = 0.5$	$a = 0.0$	$\gamma = 0.5$	$\gamma = 0.9$	$\gamma = 1.0$
1	$3.5 + 0.9$	25.061	26.579	26.972	20.763	26.655	26.972
	3.5	19.935	21.143	21.455	16.516	21.203	21.455
	3.5-0.3	18.227	19.331	19.616	15.101	19.385	19.616
2	$6.2 + 1.1$	41.579	44.098	44.748	34.448	44.223	44.748
	6.2	35.314	37.453	38.006	29.258	37.559	38.006
	6.2-0.5	32.466	34.432	34.941	26.898	34.53	34.941
3	$6.5 + 0.7$	41.009	43.494	44.135	33.977	43.617	44.135
	6.5	37.023	39.266	39.845	30.673	39.377	39.845
	6.5-0.7	33.035	35.037	35.554	27.37	35.136	35.554

estimations of the object which does not depend on observations related to its shadow. From the measured angular diameter of the shadow of M87* and assuming general relativity, the EHT Collaboration has reported the mass of the object to be $M = (6.5 \pm 0.7) \times 10^9\ M_\odot$ [65,71,72]. Therefore, this mass measurement should not be used to constrain the background metric from shadow related observations.

The above discussion reveals that the independent mass measurements of M87* (based on stellar and gas dynamics studies) differ quite substantially. Further, from Eq. (29) it is clear that the angular diameter is highly sensitive to the estimated magnitude of M. In Table I the angular diameter of M87* is estimated in both the Kerr and the JNW background assuming the different mass measurements of the object (the mass reported by the EHT Collaboration is also given for completeness), while the distance is taken to be $D = 16.8$ Mpc. From the table it is clear that the variation in mass affects the angular diameter much more than a change in the background spacetime (Table I). Moreover, for higher masses, a change in γ affects the angular diameter much more than a modification in the Kerr parameter. If independent mass estimations are not available then the angular diameter of the shadow can be used to determine the mass assuming a given background metric (as done by the EHT collaboration). In such a scenario, however, one cannot constrain the background from the angular diameter. Alternatively, without independent mass measurements the degeneracy between the mass and the background spacetime cannot be broken from the observed angular diameter of the shadow.

Although a black hole viewed at a high inclination angle can probe the background spacetime better, the present observation of M87* (viewed at $i = 17°$) can be used to throw some light on the mass of M87* and the viability of the JNW background. This is due to the greater reduction in the shadow radius in the JNW background compared to general relativity (Fig. 4 and Table I). In Fig. 6(a) we plot the variation in the angular diameter of the shadow with the JNW metric parameter γ assuming $M \sim 6.2^{+1.1}_{-0.5} \times 10^9\ M_\odot$ (the red curves) and $M \sim 3.5^{+0.9}_{-0.3} \times 10^9\ M_\odot$ (the blue curves), which are the two independent mass measurements of the object. For comparison with general relativity, the angular diameter of the shadow is also plotted against the Kerr parameter using the aforesaid masses in Fig. 6(b). In both the cases the distance is taken to be $D = 16.8$ Mpc. The angular diameter in Fig. 6 when plotted with the central value of the mass is denoted by the solid curves while the dashed curves represent the theoretical angular diameter plotted with the error bars in the masses. The pink shaded region in Fig. 6 denotes the observed angular diameter of $42 \pm 3\ \mu as$. It is important to note that since $i = 17°$ for M87*, the shadow is not exactly circular for the Kerr black hole but elongated along the y-axis. We consider the major axis (the maximum distance between two points on the circumference of the shadow [60,73]) as the shadow diameter while computing the angular diameter of the shadow.

From Fig. 6 it is clear that if $M \sim 3.5^{+0.9}_{-0.3} \times 10^9\ M_\odot$ is considered, then the observed angular diameter cannot be reproduced by merely changing the metric parameters. This mass estimation is therefore not favored by the observed shadow of M87*. In fact, even M as high as $6.2 \times 10^9\ M_\odot$ cannot explain the observed angular diameter either in general relativity or in the JNW background. This may be a plausible reason why the mass of M87* estimated by the EHT Collaboration (which is based on general relativity) is greater than both the previous estimates. Also a background metric which inherently enhances the shadow radius compared to the Kerr scenario explains the observed angular diameter of M87* better than general relativity (e.g., the braneworld scenario [60]). In the present situation, it is difficult to break the degeneracy between the presence of the black hole spin and the scalar charge if a slightly

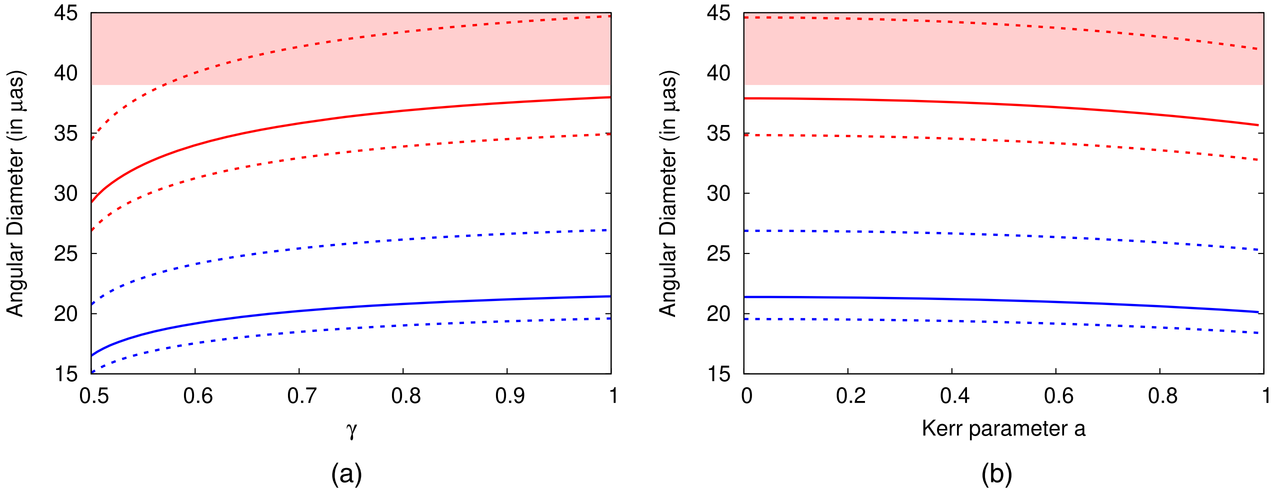

FIG. 6. The figure illustrates the variation of the angular diameter with (a) the JNW metric parameter γ and (b) the Kerr parameter a. In each of the figures, the red curves represent the angular diameter calculated with $M \sim 6.2^{+1.1}_{-0.5} \times 10^9\ M_\odot$, while the blue curves are plotted assuming $M \sim 3.5^{+0.9}_{-0.3} \times 10^9\ M_\odot$. The dashed curves in both the figues are plotted assuming the error bars in the masses about the central value. The pink shaded region represents the observed angular diameter of $42 \pm 3\ \mu as$.

higher mass is considered within the allowed range. For example, if $M \sim 6.5 \times 10^9\ M_\odot$ is used to evaluate the theoretical angular diameter then $\gamma \geq 0.85$ and $|a| \leq 0.6$ can both reproduce the observed angular diameter of M87* within the error bars. In such a scenario it is difficult to distinguish between the JNW scalar charge and the spin of the black hole from the image of M87*.

However, it is clear from Fig. 6(a) that $\gamma = 1$ (the Schwarzschild scenario) explains the observed shadow for most of the allowed values of M. In this sense the Schawarzschild scenario is more favored than the JNW spacetime and if $\gamma < 0.57$ then even $M \sim 7.3 \times 10^9\ M_\odot$ cannot address the observation. Therefore such extreme values of γ are ruled out by the present observation of the EHT collaboration. Similarly, $a = 0$ covers the maximum range of observed angular diameter in Fig. 6(b) given the allowed values of the estimated mass of the black hole.

However, M87* also exhibits a powerful jet with the jet power $P_{\mathrm{jet}} \geq 10^{42}\ \mathrm{erg\,s^{-1}}$ and if one is confined to general relativity then at least $|a| \sim 0.5$ is required to explain the jet power [71]. This estimate of a is also consistent with the shadow related observations if $6.5 \times 10^9\ M_\odot \leq M \leq 7.3 \times 10^9\ M_\odot$ is taken to compute the theoretical angular diameter [Fig. 6(b)]. Since spin plays a significant role in powering the jet, the Kerr scenario is more favored compared to the JNW spacetime if one has to also explain the observed jet power of M87*. The above discussion therefore elucidates that general relativity explains the observed angular diameter and the jet power of M87* better than the JNW background. However, it is important to note that while deriving the shadow radius we had implicitly assumed that the surrounding medium is optically thin such that the effect of the metric dominates the observed image. This may not be true and if the surrounding medium is optically thick then from the image of the surrounding accretion disk it is difficult to distinguish the JNW spacetime from the Schwarzschild metric [37].

IV. ACCRETION AROUND THE JANIS-NEWMAN-WINICOUR SPACETIME

In this section we investigate the properties of the electromagnetic emission from the accretion disk in the Janis-Newman-Winicour spacetime. The continuum spectrum emitted by the accretion disk depends not only on the nature of the background metric but also on the properties of the accretion flow. We assume the Novikov-Thorne model [74,75] for the accretion disk where the disk is considered to be geometrically thin and optically thick. Accretion takes place chiefly along the equatorial plane such that the accreting particles have large azimuthal velocity v_ϕ with negligible radial velocity v_r and even smaller vertical velocity v_z. The presence of viscosity in the system endows the accreting matter a small radial velocity which enables it to inspiral and fall into the central compact object. Within the domain of the Novikov-Thorne model the accreting matter has practically negligible v_z and hence the Novikov-Thorne accretion disk harbors “no outflows.” As the accreting matter inspirals, they lose gravitational potential energy which gets converted into electromagnetic radiation. This radiation interacts very effectively with the accreting matter and almost all of it is radiated out from the system and no heat is trapped with the accretion flow. A temperature gradient exists within the disk such that the inner disk is much hotter compared to the outer disk. Since matter and radiation interact very efficiently, every annulus of the disk emits a black body commensurate with the temperature of the disk. The integrated emission from the disk is therefore a multitemperature black body radiation. With these assumptions of the Novikov-Thorne model the flux from the accretion disk assumes an analytic form,

$$F = \frac{\dot{M}_0}{4\pi\sqrt{-g}}\tilde{f} \tag{30}$$

where,

$$\tilde{f} = -\frac{\Omega_{,r}}{(E-\Omega L)^2}\left[EL - E_{ms}L_{ms} - 2\int_{r_{ms}}^{r} LE_{,r'}dr'\right] \tag{31}$$

where, Ω, E and L are the angular velocity, specific energy and specific angular momentum of the accreting particle at the radial distance r. For a spherical symmetric metric, these can be expressed in terms of the metric parameters as,

$$\Omega = \frac{d\phi}{dt} = \frac{\sqrt{-\{g_{\phi\phi,r}\}\{g_{tt,r}\}}}{g_{\phi\phi,r}} \tag{32}$$

$$E = -u_t = \frac{-g_{tt}}{\sqrt{-g_{tt} - \Omega^2 g_{\phi\phi}}} \tag{33}$$

and

$$L = u_\phi = \frac{\Omega g_{\phi\phi}}{\sqrt{-g_{tt} - \Omega^2 g_{\phi\phi}}}. \tag{34}$$

E_{ms} and L_{ms} refer to the energy and angular momentum of the test particle at the marginally stable circular orbit. For a detailed discussion on the Novikov-Thorne model and a derivation of the expression for flux one is referred to [74–76].

Since the photon emits a Planck spectrum at every radius, the peak temperature is given by $T(r) = (\tilde{F}(r)/\sigma)^{1/4}$ where $\tilde{F}(r) = F(r)c^6/(G^2M^2)$ is the flux given in Eq. (30) obtained after bringing back the fundamental constants and σ is the Stefan Boltzmann constant.

The luminosity from the thin accretion disk is obtained by integrating the Planck function $B_\nu(T(r))$ over the disk surface at the observed frequency ν, such that,

$$L_\nu = 8\pi^2 r_g^2 \cos i \int_{r_{\rm ms}}^{r_{\rm out}} \sqrt{-g}B_\nu(T(r))dr \quad \text{and} \tag{35}$$

$$B_\nu(T) = \frac{2h\nu^3/c^2}{\exp(\frac{h\nu}{z_g kT}) - 1} \tag{36}$$

In Eq. (35), i refers to the inclination angle of the disk to the line of sight, $r_g = GM/c^2$ denotes the gravitational radius, and z_g denotes the gravitational redshift factor given by,

$$z_g = E\frac{\sqrt{-g_{tt} - \Omega^2 g_{\phi\phi}}}{E - \Omega L}. \tag{37}$$

The redshift factor takes care of the modification induced in the photon frequency while traveling from the emitting material to the observer [77].

Note that the theoretical spectrum depends chiefly on the g_{tt} component of the metric while the g_{rr} component and the volume factor is required only through the determinant of the metric [see Eq. (30), Eq. (35)] [42].

The dependence of the theoretical spectrum from the accretion disk on the metric parameter γ is illustrated in Fig. 7. We note that the presence of the scalar charge enhances the luminosity from the accretion disk for both the black hole masses (The Schwarzschild scenario is represented by the black solid line) [37]. Since the accretion rate in Eq. (30) is expressed in Eddington units, the peak temperature $T(r) \propto M^{-1/4}$ [76,78,79]. Therefore, the maximum luminosity from the accretion disk around a higher mass black hole peaks at a lower frequency.

In the next section we will estimate the observationally favored value of γ by comparing the theoretically calculated luminosity with the observed luminosity of Palomar Green quasars.

A. Observational sample

In this section, we compute the theoretical estimates of optical luminosity of a sample of Palomar Green quasars considered in [79,80] and compare these with the corresponding observed values. The masses of these quasars have been independently estimated using the method of

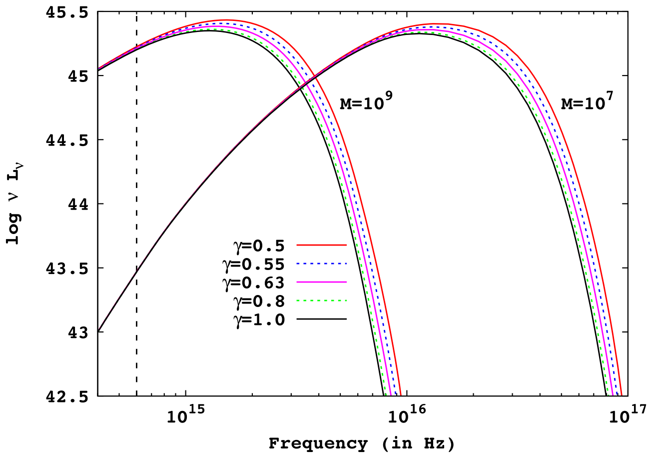

FIG. 7. The above figure illustrates variation of the theoretically derived luminosity from the accretion disk with frequency for various values of γ. The background is given by Eq. (2). The luminosity decreases with increasing γ and is minimum in the general relativistic scenario where $\gamma = 1$ (the Schwarzschild scenario). The representative masses of the black hole are taken to be $M = 10^9\ M_\odot$ and $M = 10^7\ M_\odot$. The accretion rate assumed is $1\ M_\odot\,\mathrm{yr}^{-1}$ and $\cos i$ is taken to be 0.8.

reverberation mapping [81–84]. For a subsample of thirteen quasars [79], the masses are also reported by $M-\sigma$ method [85–87]. Using observed data in the optical [88], UV [89], far-UV [90], and soft x-ray [91], the bolometric luminosities of these quasars have been estimated [79].

We calculate optical luminosity $L_{\mathrm{opt}} \equiv \nu L_\nu$ at the wavelength 4861 Å [79] for comparison with observations. For quasars the theoretical emission from the accretion disk peaks in the far-UV/extreme UV (FUV/EUV) part of the spectrum, if the Novikov-Thorne thin disk model is considered. In the observational front on the other hand, the UV region of the spectral energy distribution (SED) is not entirely contributed by the accretion disk but some physical mechanism (e.g., advection, a Comptonizing coronae, etc.) redistributes the UV flux to the x-ray frequencies [79]. Therefore, although the effect of the background metric becomes most pronounced in the UV domain for quasars, extracting the effect of the metric from UV observations become difficult due to the contamination in the UV emission from components other than the accretion disk. Moreover, the error in bolometric luminosity receives maximum contribution from the far-UV extrapolation since the uncertainty in the UV luminosity far exceeds other sources of error (e.g., optical or x-ray variability) [79]. Therefore, a comparison of the theoretically derived UV luminosities (where the spectrum peaks) with the observed UV luminosities, might lead to erroneous conclusions regarding the background spacetime, and hence we dwell in the optical domain.

We have already discussed in the previous section that the maximum disk luminosity of a lower mass black hole peaks at a higher frequency. Therefore, the peak emission from the accretion disk of a $10^9\ M_\odot$ black hole is closer to 4861 Å, the wavelength at which the analysis is done. Since the peak of the disk emission occurs very close to the marginally stable circular orbit (msco), the emission at 4861 Å comes from an inner part of the disk (closer to the msco) for a $10^9\ M_\odot$ black hole compared to a $10^7\ M_\odot$ black hole. The wavelength 4861 Å corresponds to a frequency $\sim 6\times 10^{14}$ Hz and is depicted with the dashed black vertical line in Fig. 7. Therefore, for black holes with $M\sim 10^9\ M_\odot$ the effect of the metric on the emission at 4861 Å will be more pronounced. This motivates us to consider only the quasars with $M \geq 10^9\ M_\odot$ of the sample reported in [79]. It turns out that out of eighty quasars discussed in [79], eleven quasars have a mass greater than a billion solar masses. We will consider only these quasars in this work.

Since quasars are not expected to be edge-on systems the inclination angle i is generally believed to lie between $\cos i \in (0.5, 1)$. In this work we adopt a typical value of $\cos i \sim 0.8$ in our analysis [79,92]. It turns out that for nonrotating black holes the error (e.g., reduced χ^2, Nash-Sutcliffe efficiency, index of agreement etc.) between the theoretical and observed luminosities get minimized when cosi lies between 0.77–0.82 [93]. Moreover, Piotrovich *et al.* [94] estimated the inclination angles of some of the quasars in our sample which turns out to be consistent with our choice.

The accretion rates of the quasars are reported in [79]. The accretion rates in [79] are estimated based on a stellar-atmosphere-like model (referred to as TLUSTY models) with black hole spin $a/M = 0.9$. However, if a blackbody model with spin $a/M = 0$ is used, then for larger M the accretion rates are expected to exhibit a maximum increase by 40% while for smaller M the accretion rates tend to be smaller by 20% compared to the accretion rates reported in [79]. In order to take this factor into account we vary the accretion rates between 80% to 140% of the reported accretion rates [79] for each quasar in the subsample (with $M \geq 10^9\ M_\odot$), while performing the error estimations.

B. Numerical analysis and error estimators

In this section we compute several error estimators which will enable us to deduce the observationally favored model of γ.

(i) Chi-square $\boldsymbol{\chi}^2$: Consider a set of observed data $\{\mathcal{O}_i\}$ with possible errors $\{\sigma_i\}$. The corresponding model estimates of the observed quantity is denoted by $\Omega_i(\gamma)$, where γ is related to the scalar charge associated with each of the quasars. The χ^2 of the distribution is then given by,

$$\chi^2(\gamma) = \sum_i \frac{\{\mathcal{O}_i - \Omega_i(\gamma)\}^2}{\sigma_i^2} \tag{38}$$

In Eq. (38), σ_i refers to the error associated with the observed optical luminosity for each of the quasars. It turns out that the error in optical luminosity is negligible compared to the error in bolometric luminosity which receives maximum contribution from the far-UV extrapolation as the uncertainty in the UV luminosity far exceeds other sources of error (e.g.,

TABLE II. The mass, accretion rate, optical, and bolometric luminosity of the eleven quasars considered are reported. These are taken from [79].

Object	$\mathcal{M}_0$	log M_0	log $\mathrm{L}_{\mathrm{opt}}$	log $\mathrm{L}_{\mathrm{bol}}$
0003 + 158	9.16	0.79	45.87	46.92 ± 0.25
1048 − 090	9.01	0.30	45.45	46.57 ± 0.32
1100 + 772	9.13	0.29	45.51	46.61 ± 0.25
1103 − 006	9.08	0.21	45.43	46.19 ± 0.10
1216 + 069	9.06	0.51	45.62	46.61 ± 0.28
1226 + 023	9.01	1.18	46.03	47.09 ± 0.24
1425 + 267	9.53	0.07	45.55	46.35 ± 0.20
1512 + 370	9.20	0.20	45.48	47.11 ± 0.50
1545 + 210	9.10	0.01	45.29	46.14 ± 0.13
1704 + 608	9.29	0.38	45.65	46.67 ± 0.21
2308 + 098	9.43	0.22	45.62	46.61 ± 0.22

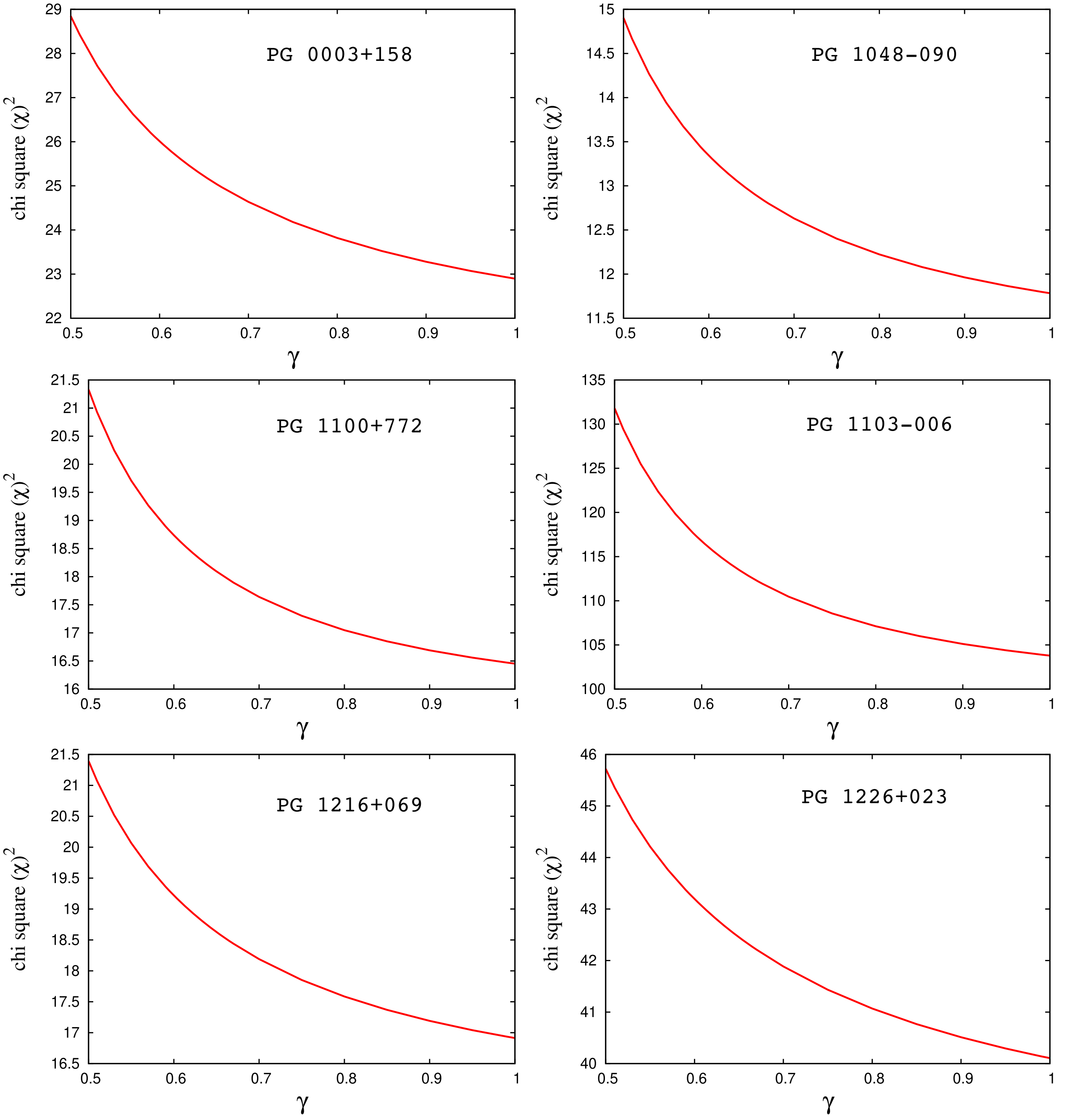

FIG. 8. The above figure depicts variation of χ^2 as a function of the metric parameter γ for individual quasars with $M \geq 10^9\ M_\odot$. For every quasar an uncertainty of $0.4dex$ is considered in the mass while accretion rates are varied between 80% to 140% of the value reported in [79], to compute the theoretical luminosity. It is evident from the plot that χ^2 minimizes for $\gamma \sim 1$. For more discussion see text.

optical or x-ray variability) [79]. Since the errors in optical luminosity of the quasars are not explicitly reported we consider the errors in the bolometric luminosity (reported in [79] and Table II) as the maximum error possible in the estimation of the optical luminosity.

In order to compute the χ^2, the theoretical estimate of optical luminosity Ω_i is required, which depends on the mass of the quasars, their accretion rates and the metric parameter γ (which is related to the scalar charge associated with the black hole). As discussed in the last section we consider eleven quasars with mass $M \geq 10^9\ M_\odot$ [79] in our analysis. For each of these quasars, the masses based on reverberation mapping are reported in [79] (also mentioned in Table II) which are subject to systematic errors that

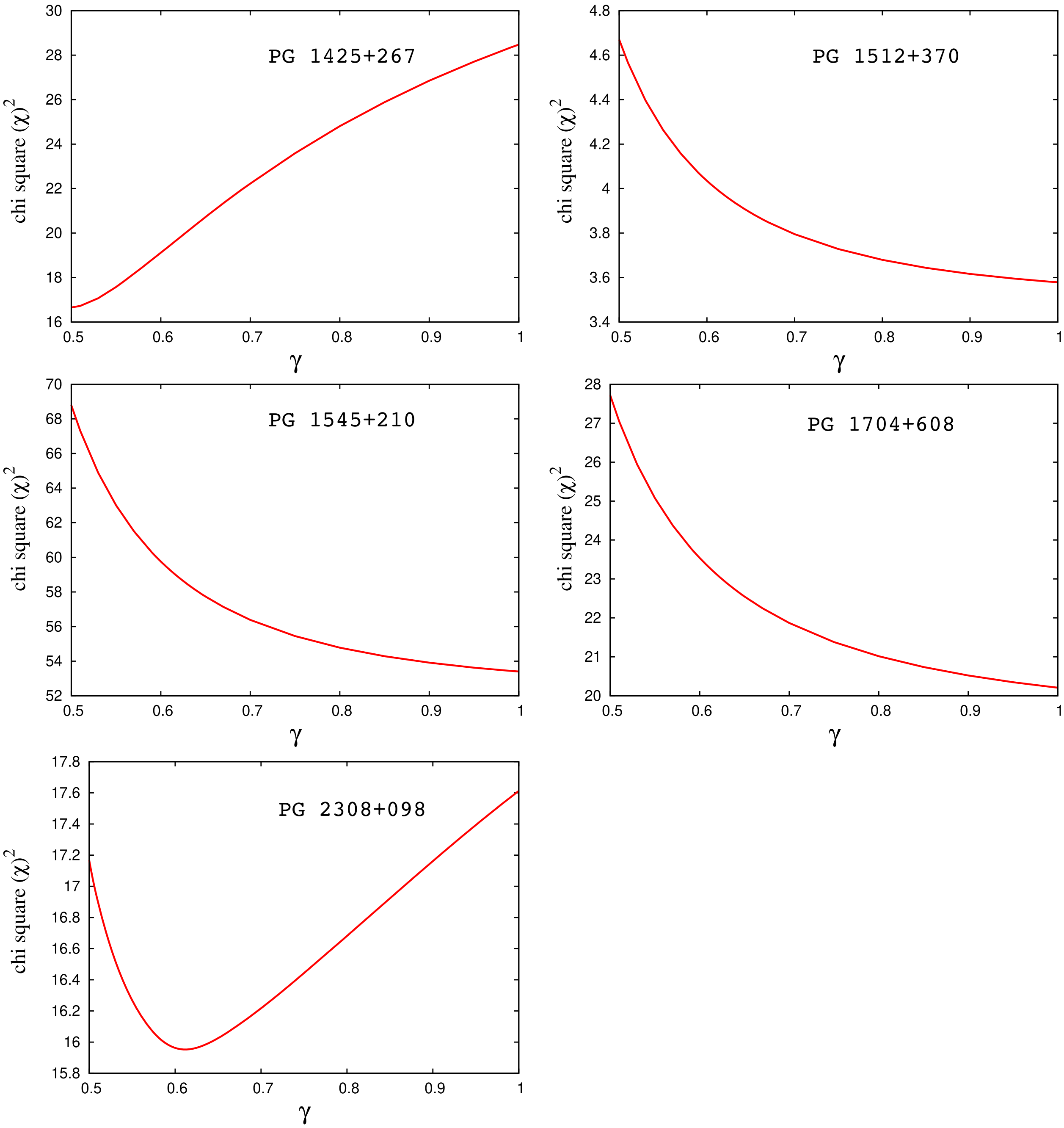

FIG. 9. The above figure depicts variation of χ^2 as a function of the metric parameter γ for individual quasars with $M \geq 10^9\ M_\odot$. While computing the χ^2 for a given value of γ an uncertainty of $0.4dex$ is considered in the mass estimates for all quasars while accretion rates are varied between 80% to 140% of the value reported in [79], to compute the theoretical luminosity. The figure illustrates that for most quasars χ^2 minimizes for $\gamma \sim 1$, the exceptions being PG $1425+267$ and PG $2308+098$.

override the statistical uncertainty in the input data. The systematic errors are difficult to quantify and a factor of ~3 (0.4 dex) error is considered as the characteristic uncertainty in the mass estimates [79]. For example, the mass of the quasar PG $1545+210$ is taken to be $\log \mathrm{M} = 9.10 \pm 0.4\ M_\odot$. We denote the central value of the logarithm of the mass by $\mathcal{M}_0$ (reported in Table II). Then in the logarithmic scale the mass M of the quasars can vary between $\mathcal{M}_0 - 0.4 \lesssim \log \mathrm{M} \lesssim \mathcal{M}_0 + 0.4$. For example, for PG $1545+210$, $\mathcal{M}_0 = 9.10$. The accretion rates of these quasars can at most vary between 80% to 140% of the accretion rate reported in Table II (see discussion in the last section), which can be used to compute the theoretical luminosity. For easier reference, the mass, accretion rate, optical, and bolometric luminosities of the eleven PG quasars are reported in Table II.

In order to compute the χ^2 for a given source with central value of the logarithm of its mass $\mathcal{M}_0$, we first fix a value of γ in the range 0.5 to 1. Then we fix the value of mass in the range $\mathcal{M}_0 - 0.4 \lesssim \log \mathrm{M} \lesssim \mathcal{M}_0 + 0.4$ and allow the accretion rate to vary between 0.8 to 1.4 times the accretion rate $\dot{M}_0$ reported in Table II in steps of 0.1. For each different accretion rate, but fixed log M and γ, we compute the theoretical optical luminosity and subsequently the χ^2 as in Eq. (38) and simply sum them up. While computing the χ^2 the error in the observed optical luminosity σ_i is required. As mentioned earlier in this section, σ_i is taken to be the error in the bolometric luminosity (reported in Table II) as the maximum error possible in the estimation of the optical luminosity. This method therefore considers the effect of variation in the accretion rate.

Next we consider a different value of log M for the same quasar in the allowed range mentioned above, keep the γ fixed, but vary the accretion rate as before, compute the resultant χ^2 and again add them up to the previous sum of χ^2. We repeat this procedure for all values of log M in the aforesaid range, where the stepsize of varying log M is also taken to be 0.1. In this way χ^2 for a particular magnitude of γ is calculated which is essentially the sum of the χ^2 obtained by varying the mass and the accretion rate.

Now the last two steps are repeated for all $\gamma \in (0.5, 1)$ to obtain the variation of χ^2 with γ for the given source. Subsequently, the above process is reiterated for all the eleven quasars which gives the dependence of the χ^2 on γ for the individual quasars. In Figs. 8 and 9 we plot the variation of χ^2 with γ for each of the eleven quasars. We note that for most of the quasars the χ^2 minimizes for $\gamma \approx 1$ except for PG $1425 + 267$ and PG $2308 + 098$. This indicates that the Schwarzschild scenario is mostly favored by optical observations of quasars compared to the Janis Newman Winicour spacetime.

We next compute the joint chi-square by summing the χ^2 of all the quasars for a given value of γ, and repeating this process for all γ in the physically allowed range $\gamma \in (0.5, 1)$. This is depicted in Fig. 10 which illustrates that the total χ^2 minimizes for $\gamma \approx 1$, thereby favoring the Schwarzschild scenario. In order to strengthen our conclusions we consider a few more error estimators. In the remaining error estimators, the theoretical luminosity is computed with masses of the quasars from Table II while accretion rates considered are 1.4 times the accretion rate reported in Table II. This is because we are considering the quasars in the high mass end ($M \geq 10^9\ M_\odot$) [79] (discussion in Sec. IVA).

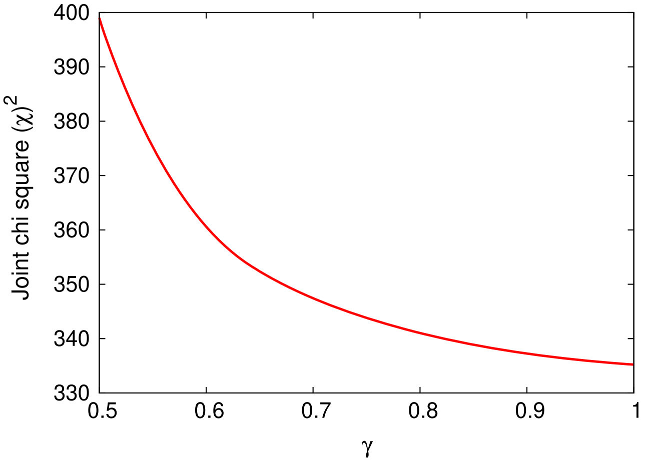

FIG. 10. The above figure depicts the joint χ^2 (by summing the χ^2 for all the quasars) as a function of the metric parameter γ. It is evident from the plot that χ^2 minimizes for $\gamma \sim 1.0$.

(ii) Nash-Sutcliffe efficiency and its modified form: Nash-Sutcliffe Efficiency E [95–97] is related to the sum of the squared differences between the observed and the predicted values normalized by the variance of the observed values. This error estimator assumes the form,

$$E(\gamma) = 1 - \frac{\sum_i \{\mathcal{O}_i - \Omega_i(\gamma)\}^2}{\sum_i \{\mathcal{O}_i - \mathcal{O}_{av}\}^2} \tag{39}$$

where $\mathcal{O}_{\mathrm{av}}$ denotes average of the observed values of the optical luminosities of the quasars. Unlike χ^2, the model which best describes the observation maximizes the Nash-Sutcliffe efficiency. A model with $E \sim 1$ is considered to be an ideal model that accurately predicts the observations. While calculating the theoretical optical luminosity for a given γ in Eq. (39), the masses of the quasars are considered from Table 1 of [79] while the accretion rates are multiplied by a factor of 1.4 since we are considering the quasars in the high mass end ($M \geq 10^9\ M_\odot$) [79]. This choice of mass and accretion rate is taken for every quasar in the remaining error estimators we discuss further.

As depicted in Fig. 11(a) in our case, E maximizes for $\gamma \sim 1$, indicating that the Schwarzschild scenario predicts the observation better than the Janis Newman Winicour background.

Nash-Sutcliffe efficiency E tends to be oversensitive to higher values of the luminosity for taking square of the error in the numerator [see, e.g., Eq. (39)]. Therefore, a modified version of the Nash-Sutcliffe efficiency denoted by E_1 [96] is used, where,

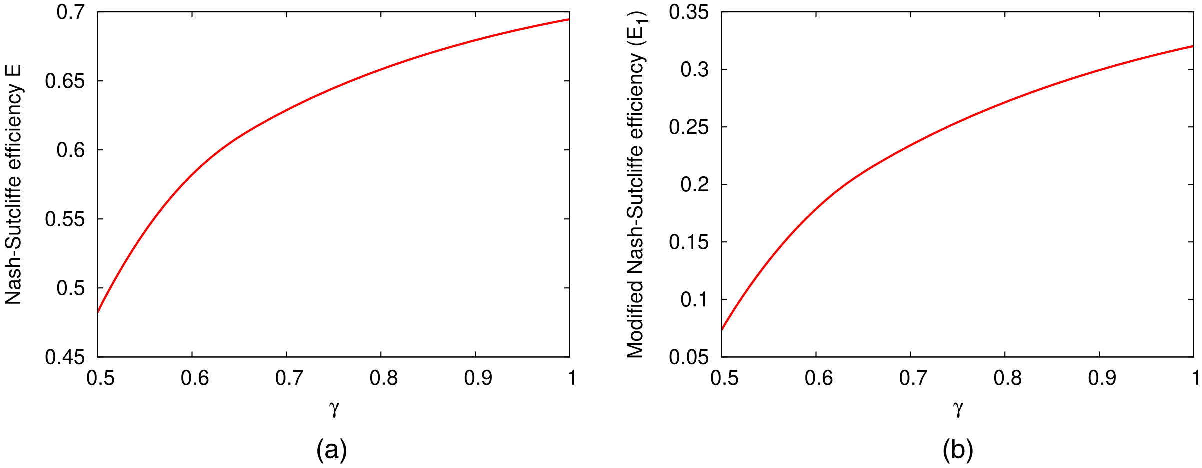

FIG. 11. The above figure depicts variation of (a) the Nash-Sutcliffe efficiency E and (b) the modified form of the Nash-Sutcliffe efficiency E_1 with the metric parameter γ. Both the error estimators maximize for $\gamma \sim 1$.

$$E_1(\gamma) = 1 - \frac{\sum_i |\mathcal{O}_i - \Omega_i(\gamma)|}{\sum_i |\mathcal{O}_i - \mathcal{O}_{\rm av}|}. \tag{40}$$

Similar to E, a model which maximizes E_1 is considered to be a better description of the data. Figure 11(b) illustrates that E_1 maximizes for $\gamma \sim 1$. The conclusions drawn from these two error estimators corroborate our previous findings.

(iii) Index of agreement and its modified form: The index of agreement was proposed [97–99] to overcome the insensitivity of the Nash-Sutcliffe efficiency and its modified form toward the differences between the observed and predicted means and variances. Denoted by d, it assumes the form,

$$d(\gamma) = 1 - \frac{\sum_i \{\mathcal{O}_i - \Omega_i(\gamma)\}^2}{\sum_i \{|\mathcal{O}_i - \mathcal{O}_{av}| + |\Omega_i(\gamma) - \mathcal{O}_{av}|\}^2} \tag{41}$$

The denominator, which denotes the maximum deviation of each pair of observed and predicted luminosities from the average luminosity is known as the potential error.

Similar to Nash-Sutcliffe efficiency, the index of agreement suffers from oversensitivity to higher values of optical luminosity due to the presence of the squared luminosities in the numerator of Eq. (41) and hence its modified version d_1 is proposed, where,

$$d_1(\gamma) = 1 - \frac{\sum_i |\mathcal{O}_i - \Omega_i(\gamma)|}{\sum_i \{|\mathcal{O}_i - \mathcal{O}_{av}| + |\Omega_i(\gamma) - \mathcal{O}_{av}|\}} \tag{42}$$

Similar to the previous error estimators, we note from Fig. 12(a) and Fig. 12(b) that the model which best describes the observation maximizes d and d_1 and hence corresponds to $\gamma \sim 1$. Therefore, the conclusions drawn previously remain unaltered, i.e., the

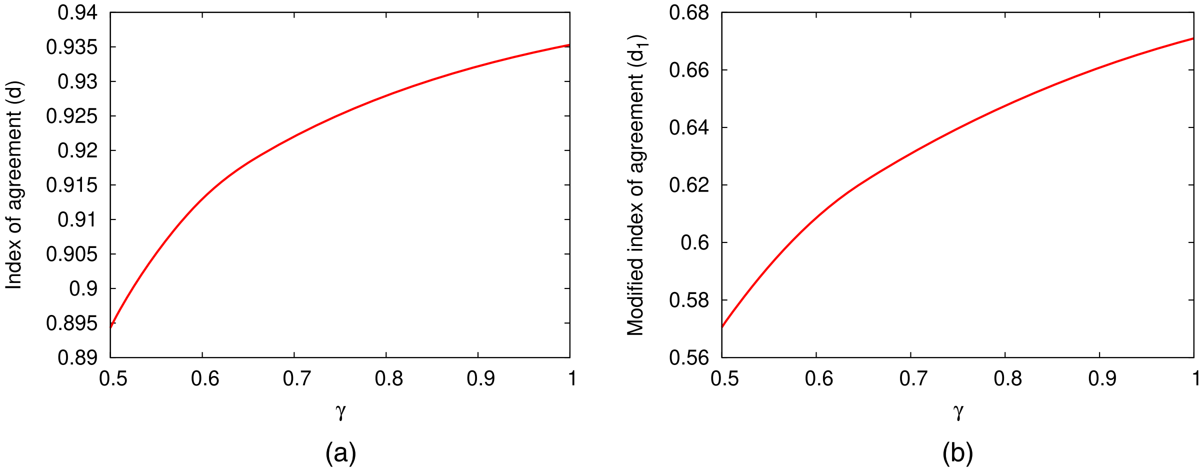

FIG. 12. The above figure depicts variation of (a) index of agreement d and (b) the modified index of agreement $\mathbf{d}_1$ with the metric parameter γ. Both the error estimators maximize for $\gamma \sim 1$ favoring the Schwarzschild scenario.

Schwarzschild scenario seems to be favored by optical observations of quasars compared to the Janis-Newman-Winicour spacetime.

V. CONCLUSION

The main goal of this work is to explore the characteristics of electromagnetic observations in the Janis-Newman-Winicour spacetime and confront them with the available observational data. This naturally involves investigating the nature of the black hole shadow and accretion in this background. Below we enlist the important results of this work:

(i) While investigating the properties of the shadow, we note that the presence of the scalar charge decreases the effects of the gravitational lensing and diminishes the shadow radius compared to the Schwarzschild scenario. With the increase in scalar charge or decrease in γ the radius of the photon sphere increases while that of the shadow decreases which is one of the unique properties of the Janis-Newman-Winicour spacetime. A spinning black hole also casts a smaller shadow compared to a Schwarzschild black hole, although the scalar charge causes a greater reduction in the shadow radius compared to the Kerr scenario. This feature can partially remove the degeneracy between the JNW metric parameter γ and the spin, from the recently observed image of M87*. Given the uncertainty in the mass estimates of the object, the observed angular diameter of M87* can be reproduced within the error bars, both by $\gamma \geq 0.57$ and any magnitude of the Kerr parameter (Fig. 6). However, the Schwarzschild scenario explains the observed shadow for most of the allowed values of M and in this way the Schwarzschild scenario is more favored by the observed shadow of M87*. Also extreme values of γ ($\gamma < 0.57$) are completely ruled out by the first image of the black hole, purely based on its small angular diameter. Moreover, M87* also exhibits a powerful jet with $P_{\mathrm{jet}} \geq 10^{42}\ \mathrm{erg\,s^{-1}}$ and $|a| \geq 0.5$ is required to explain the requisite jet power [71]. This estimate of $|a|$ is also consistent with the shadow related observation, given the uncertainties in its mass estimate. Therefore, the observed jet further corroborates general relativity over the JNW spacetime. A future observation of a black hole viewed at a high inclination angle and having precise and independent estimations of its mass and distance can be further used to establish/falsify the viability of the JNW spacetime.

(ii) In the Winicour solution when the metric parameters γ and b are treated as independent, a new regime emerges where b is negative and $\gamma \leq -0.5$. This represents a horizonless compact object with real positive solutions for photon sphere and shadow. This is an interesting generalization in the parameter space of the Janis-Newman-Winicour spacetime which has not been discussed much in the literature.

(iii) Apart from studying the nature of the shadow in the Janis-Newman-Winicour spacetime, we also explore the effects of this background on the accretion onto the compact object. We compute the theoretical estimates of optical luminosity from the accretion disk for a sample of Palomar Green quasars with $M \geq 10^9\ M_\odot$ [79] and compare them with the corresponding observations. The uncertainties associated with the mass and the accretion rates are taken into account while computing the theoretical luminosity from the accretion disk which are subsequently used to evaluate the error estimators. For every allowed magnitude of mass and accretion rate, the variation of χ^2 with γ is computed for all the quasars. It turns out that the χ^2 minimizes in the Schwarzschild scenario for most of the quasars, thereby favoring general relativity over the JNW background. This is eventually followed by evaluating the joint-χ^2 and other error estimators like the Nash-Sutcliffe efficiency, the index of agreement etc., which in turn supports our earlier findings. This result is also in agreement with the first observed shadow of a black hole which is another independent window to test the nature of strong gravity in the electromagnetic domain.

It is however important to mention that the quasars are multicomponent systems containing the accretion disk, the corona, the jet, and the dusty torus emitting in all bands of the electromagnetic spectrum and we have not explicitly fitted the observed SED with the Novikov-Thorne model which mimics the emission only from the accretion disk. We are interested in disentangling the effect of the background metric from the SED and only emissions from regions very close to the black hole gets modified by the background spacetime. This is one of the primary reasons we choose to model the accretion disk since the effect of the metric on the other components is not so important. Second, modeling the entire spectral energy distribution (SED) theoretically is extremely challenging since it depends not only on the background spacetime but also on the properties of the accretion flow and one often resorts to phenomenological models to address this issue. Discerning the effect of the metric from the SED therefore becomes quite nontrivial. Our goal in this work is not to model the entire SED but to constrain the value of γ from the accretion observations using a theoretical model for the disk. Among the available theoretical models the Novikov-Thorne model is very successful in explaining the emission from the accretion disk and our work is simply a first attempt to identify the observationally favored value of the scalar charge of the JNW spacetime from the accretion data.

ACKNOWLEDGMENTS

The research of S. S. G. is partially supported by the Science and Engineering Research Board-Extra Mural Research Grant No. (EMR/2017/001372), Government of India. The research of S. S. is funded by CSIR, Government of India.

[1] P. S. Joshi and I. H. Dwivedi, Naked singularities in spherically symmetric inhomogeneous Tolman-Bondi dust cloud collapse, Phys. Rev. D **47**, 5357 (1993).

[2] B. Waugh and K. Lake, Strengths of shell focusing singularities in marginally bound collapsing selfsimilar Tolman space-times, Phys. Rev. D **38**, 1315 (1988).

[3] D. Christodoulou, Violation of cosmic censorship in the gravitational collapse of a dust cloud, Commun. Math. Phys. **93**, 171 (1984).

[4] D. M. Eardley and L. Smarr, Time function in numerical relativity. Marginally bound dust collapse, Phys. Rev. D **19**, 2239 (1979).

[5] A. Ori and T. Piran, Naked Singularities in Self-Similar Spherical Gravitational Collapse, Phys. Rev. Lett. **59**, 2137 (1987).

[6] R. Giambo, F. Giannoni, G. Magli, and P. Piccione, Naked singularities in the gravitational collapse of barotropic spherical fluids, Gen. Relativ. Gravit. **36**, 1279 (2004).

[7] S. L. Shapiro and S. A. Teukolsky, Formation of Naked Singularities: The Violation of Cosmic Censorship, Phys. Rev. Lett. **66**, 994 (1991).

[8] K. Lake, Naked singularities in gravitational collapse which is not self-similar, Phys. Rev. D **43**, 1416 (1991).

[9] R. Goswami and P. S. Joshi, Spherical gravitational collapse in N-dimensions, Phys. Rev. D **76**, 084026 (2007).

[10] P. S. Joshi, N. Dadhich, and R. Maartens, Why do naked singularities form in gravitational collapse?, Phys. Rev. D **65**, 101501 (2002).

[11] T. Harada, H. Iguchi, and K.-i. Nakao, Naked singularity formation in the collapse of a spherical cloud of counter rotating particles, Phys. Rev. D **58**, 041502 (1998).

[12] R. Penrose, Gravitational collapse: The role of general relativity, Riv. Nuovo Cimento **1**, 252 (1969); Gen. Relativ. Gravit. **34**, 1141 (2002).

[13] Z. Kovacs and T. Harko, Can accretion disk properties observationally distinguish black holes from naked singularities?, Phys. Rev. D **82**, 124047 (2010).

[14] M. Blaschke and Z. Stuchlík, Efficiency of the Keplerian accretion in braneworld Kerr-Newman spacetimes and mining instability of some naked singularity spacetimes, Phys. Rev. D **94**, 086006 (2016).

[15] Z. Stuchlik and J. Schee, Appearance of Keplerian discs orbiting Kerr superspinars, Classical Quantum Gravity **27**, 215017 (2010).

[16] C. Bambi, K. Freese, T. Harada, R. Takahashi, and N. Yoshida, Accretion process onto super-spinning objects, Phys. Rev. D **80**, 104023 (2009).

[17] P. S. Joshi, D. Malafarina, and R. Narayan, Equilibrium configurations from gravitational collapse, Classical Quantum Gravity **28**, 235018 (2011).

[18] D. Pugliese, H. Quevedo, and R. Ruffini, Equatorial circular motion in Kerr spacetime, Phys. Rev. D **84**, 044030 (2011).

[19] P. Pradhan and P. Majumdar, Circular orbits in extremal reissner Nordstrom spacetimes, Phys. Lett. A **375**, 474 (2011).

[20] K. Hioki and K.-i. Maeda, Measurement of the Kerr spin parameter by observation of a compact object’s shadow, Phys. Rev. D **80**, 024042 (2009).

[21] L. Yang and Z. Li, Shadow of a dressed black hole and determination of spin and viewing angle, Int. J. Mod. Phys. D **25**, 1650026 (2016).

[22] R. Takahashi, Shapes and positions of black hole shadows in accretion disks and spin parameters of black holes, J. Korean Phys. Soc. **45**, S1808 (2004); Astrophys. J. **611**, 996 (2004).

[23] G. N. Gyulchev and S. S. Yazadjiev, gravitational lensing by rotating naked singularities, Phys. Rev. D **78**, 083004 (2008).

[24] K. S. Virbhadra and G. F. R. Ellis, Gravitational lensing by naked singularities, Phys. Rev. D **65**, 103004 (2002).

[25] K. S. Virbhadra, D. Narasimha, and S. M. Chitre, Role of the scalar field in gravitational lensing, Astron. Astrophys. **337**, 1 (1998), http://adsabs.harvard.edu/full/1998A%26A...337....1V.

[26] K. S. Virbhadra and C. R. Keeton, Time delay and magnification centroid due to gravitational lensing by black holes and naked singularities, Phys. Rev. D **77**, 124014 (2008).

[27] M. Patil and P. S. Joshi, High energy particle collisions in superspinning Kerr geometry, Phys. Rev. D **84**, 104001 (2011).

[28] R. Shaikh, Shadows of rotating wormholes, Phys. Rev. D **98**, 024044 (2018).

[29] P. V. P. Cunha, C. A. R. Herdeiro, and M. J. Rodriguez, Does the black hole shadow probe the event horizon geometry?, Phys. Rev. D **97**, 084020 (2018).

[30] G. Gyulchev, P. Nedkova, V. Tinchev, and S. Yazadjiev, On the shadow of rotating traversable wormholes, Eur. Phys. J. C **78**, 544 (2018).

[31] P. G. Nedkova, V. K. Tinchev, and S. S. Yazadjiev, Shadow of a rotating traversable wormhole, Phys. Rev. D **88**, 124019 (2013).

[32] A. I. Janis, E. T. Newman, and J. Winicour, Reality of the Schwarzschild Singularity, Phys. Rev. Lett. **20**, 878 (1968).

[33] I. Z. Fisher, Scalar mesostatic field with regard for gravitational effects, Zh. Eksp. Teor. Fiz. **18**, 636 (1948).
[34] K. A. Bronnikov and A. V. Khodunov, Scalar field and gravitational instability, Gen. Relativ. Gravit. **11**, 13 (1979).
[35] M. Wyman, Static spherically symmetric scalar fields in general relativity, Phys. Rev. D **24**, 839 (1981).
[36] K. S. Virbhadra, Janis-Newman-Winicour, and Wyman solutions are the same, Int. J. Mod. Phys. A **12**, 4831 (1997).
[37] G. Gyulchev, P. Nedkova, T. Vetsov, and S. Yazadjiev, Image of the Janis-Newman-Winicour naked singularity with a thin accretion disk, Phys. Rev. D **100**, 024055 (2019).
[38] A. N. Chowdhury, M. Patil, D. Malafarina, and P. S. Joshi, Circular geodesics and accretion disks in Janis-Newman-Winicour and Gamma metric, Phys. Rev. D **85**, 104031 (2012).
[39] A. I. Janis, E. T. Newman, and J. Winicour, Reality of the Schwarzschild Singularity, Phys. Rev. Lett. **20**, 878 (1968).
[40] M. Wyman, Static spherically symmetric scalar fields in general relativity, Phys. Rev. D **24**, 839 (1981).
[41] S. Kar, S. SenGupta, and S. Sur, Static spherisymmetric solutions, gravitational lensing and perihelion precession in Einstein-Kalb-Ramond theory, Phys. Rev. D **67**, 044005 (2003).
[42] I. Banerjee, B. Mandal, and S. SenGupta, In quest of axionic hairs in quasars, J. Cosmol. Astropart. Phys. 03 (2018) 039.
[43] I. Banerjee, S. Sau, and S. SenGupta, Implications of axionic hair on shadow of M87*, Phys. Rev. D **101**, 104057 (2020).
[44] Z. Stuchlik and A. Kotrlova, Orbital resonances in discs around braneworld Kerr black holes, Gen. Relativ. Gravit. **41**, 1305 (2009).
[45] C. Bambi, A code to compute the emission of thin accretion disks in non-Kerr space-times and test the nature of black hole candidates, Astrophys. J. **761**, 174 (2012).
[46] C. Liu, T. Zhu, Q. Wu, K. Jusufi, M. Jamil, M. Azreg-Aïnou, and A. Wang, Shadow and quasinormal modes of a rotating loop quantum black hole, Phys. Rev. D **101**, 084001 (2020).
[47] C. Liu, T. Zhu, and Q. Wu, Thin accretion disk around a four-dimensional Einstein-Gauss-Bonnet black hole, arXiv: 2004.01662.
[48] T. Zhu, Q. Wu, M. Jamil, and K. Jusufi, Shadows and deflection angle of charged and slowly rotating black holes in Einstein-Æther theory, Phys. Rev. D **100**, 044055 (2019).
[49] K. Chakravarti, S. Chakraborty, K. S. Phukon, S. Bose, and S. SenGupta, Constraining extra-spatial dimensions with observations of GW170817, Classical Quantum Gravity **37**, 105004 (2020).
[50] S. Chakraborty, K. Chakravarti, S. Bose, and S. SenGupta, Signatures of extra dimensions in gravitational waves from black hole quasinormal modes, Phys. Rev. D **97**, 104053 (2018).
[51] L. Visinelli, N. Bolis, and S. Vagnozzi, Brane-world extra dimensions in light of GW170817, Phys. Rev. D **97**, 064039 (2018).
[52] P. V. P. Cunha and C. A. R. Herdeiro, Shadows and strong gravitational lensing: A brief review, Gen. Relativ. Gravit. **50**, 42 (2018).
[53] A. de Vries, The apparent shape of a rotating charged black hole, closed photon orbits and the bifurcation setA4, Classical Quantum Gravity **17**, 123 (2000).
[54] S. E. Gralla, D. E. Holz, and R. M. Wald, Black hole shadows, photon rings, and lensing rings, Phys. Rev. D **100**, 024018 (2019).
[55] A. A. Abdujabbarov, L. Rezzolla, and B. J. Ahmedov, A coordinate-independent characterization of a black hole shadow, Mon. Not. R. Astron. Soc. **454**, 2423 (2015).
[56] A. Abdujabbarov, M. Amir, B. Ahmedov, and S. G. Ghosh, Shadow of rotating regular black holes, Phys. Rev. D **93**, 104004 (2016).
[57] C. Bambi, K. Freese, S. Vagnozzi, and L. Visinelli, Testing the rotational nature of the supermassive object M87* from the circularity and size of its first image, Phys. Rev. D **100**, 044057 (2019).
[58] S. Vagnozzi and L. Visinelli, Hunting for extra dimensions in the shadow of M87*, Phys. Rev. D **100**, 024020 (2019).
[59] A. Allahyari, M. Khodadi, S. Vagnozzi, and D. F. Mota, Magnetically charged black holes from non-linear electrodynamics and the Event Horizon Telescope, J. Cosmol. Astropart. Phys. 02 (2020) 003.
[60] I. Banerjee, S. Chakraborty, and S. SenGupta, Silhouette of M87*: A new window to peek into the world of hidden dimensions, Phys. Rev. D **101**, 041301 (2020).
[61] R. Roy and U. A. Yajnik, Evolution of black hole shadow in the presence of ultralight bosons, Phys. Lett. B **803**, 135284 (2020).
[62] B. Carter, Global structure of the Kerr family of gravitational fields, Phys. Rev. **174**, 1559 (1968).
[63] J. M. Bardeen, in *Black Holes (Les Astres Occlus)*, edited by C. Dewitt and B. S. Dewitt (Gordon and Breach Science Publishers, New York, 1973), p. 215.
[64] E. Teo, Spherical photon orbits around a kerr black hole, Gen. Relativ. Gravit. **35**, 1909 (2003).
[65] K. Akiyama *et al.* (Event Horizon Telescope Collaboration), First M87 event horizon telescope results. I. The shadow of the supermassive black hole, Astrophys. J. **875**, L1 (2019).
[66] J. P. Blakeslee, A. Jordan, S. Mei, P. Cote, L. Ferrarese, L. Infante, E. W. Peng, J. L. Tonry, and M. J. West, The ACS Fornax cluster survey. V. Measurement and recalibration of surface brightness fluctuations and a precise value of the Fornax–Virgo relative distance, Astrophys. J. **694**, 556 (2009).
[67] S. Bird, W. E. Harris, J. P. Blakeslee, and C. Flynn, The inner halo of M87: A first direct view of the red-giant population, Astron. Astrophys. **524**, A71 (2010).
[68] M. Cantiello *et al.*, A precise distance to the host galaxy of the binary neutron star merger GW170817 using surface brightness fluctuations, Astrophys. J. **854**, L31 (2018).
[69] K. Gebhardt, J. Adams, D. Richstone, T. R. Lauer, S. M. Faber, K. Gultekin, J. Murphy, and S. Tremaine, The black-hole mass in M87 from Gemini/NIFS adaptive optics observations, Astrophys. J. **729**, 119 (2011).
[70] J. L. Walsh, A. J. Barth, L. C. Ho, and M. Sarzi, The M87 black hole mass from gas-dynamical models of space telescope imaging spectrograph observations, Astrophys. J. **770**, 86 (2013).

[71] K. Akiyama *et al.* (Event Horizon Telescope Collaboration), First M87 Event Horizon Telescope results. V. Physical origin of the asymmetric ring, Astrophys. J. **875**, L5 (2019).

[72] K. Akiyama *et al.* (Event Horizon Telescope Collaboration), First M87 event horizon telescope results. VI. The shadow and mass of the central black hole, Astrophys. J. **875**, L6 (2019).

[73] S.-W. Wei, Y.-C. Zou, Y.-X. Liu, and R. B. Mann, Curvature radius and Kerr black hole shadow, J. Cosmol. Astropart. Phys. 08 (2019) 030.

[74] I. D. Novikov and K. S. Thorne, Astrophysics of black holes, in *Black Holes (Les Astres Occlus)*, edited by C. Dewitt and B. S. Dewitt (Gordon and Breach, New York, 1973), pp. 343–450.

[75] D. N. Page and K. S. Thorne, Disk-accretion onto a black hole. time-averaged structure of accretion disk, Astrophys. J. **191**, 499 (1974).

[76] I. Banerjee, S. Chakraborty, and S. SenGupta, Decoding signatures of extra dimensions and estimating spin of quasars from the continuum spectrum, Phys. Rev. D **100**, 044045 (2019).

[77] D. Ayzenberg and N. Yunes, Black hole continuum spectra as a test of general relativity: Quadratic gravity, Classical Quantum Gravity **34**, 115003 (2017).

[78] J. Frank, A. King, and D. J. Raine, *Accretion Power in Astrophysics: Third Edition* (Cambridge University Press, Cambridge, England, 2002).

[79] S. W. Davis and A. Laor, The radiative efficiency of accretion flows in individual AGN, Astrophys. J. **728**, 98 (2011).

[80] M. Schmidt and R. F. Green, Quasar evolution derived from the Palomar bright quasar survey and other complete quasar surveys, Astrophys. J. **269**, 352 (1983).

[81] S. Kaspi, P. S. Smith, H. Netzer, D. Maoz, B. T. Jannuzi, and U. Giveon, Reverberation measurements for 17 quasars and the size mass luminosity relations in active galactic nuclei, Astrophys. J. **533**, 631 (2000).

[82] S. Kaspi, D. Maoz, H. Netzer, B. M. Peterson, M. Vestergaard, and B. T. Jannuzi, The relationship between luminosity and broad-line region size in active galactic nuclei, Astrophys. J. **629**, 61 (2005).

[83] T. A. Boroson and R. F. Green, The emission-line properties of low-redshift quasi-stellar objects, Astrophys. J. Suppl. **80**, 109 (1992), https://ui.adsabs.harvard.edu/abs/1992ApJS..80..109B/abstract.

[84] B. M. Peterson *et al.*, Central masses and broad-line region sizes of active galactic nuclei. II. A homogeneous analysis of a large reverberation-mapping database, Astrophys. J. **613**, 682 (2004).

[85] L. Ferrarese and D. Merritt, A fundamental relation between supermassive black holes and their host galaxies, Astrophys. J. **539**, L9 (2000).

[86] K. Gebhardt *et al.*, A relationship between nuclear black hole mass and galaxy velocity dispersion, Astrophys. J. **539**, L13 (2000).

[87] S. Tremaine *et al.*, The slope of the black hole mass versus velocity dispersion correlation, Astrophys. J. **574**, 740 (2002).

[88] G. Neugebauer, R. F. Green, K. Matthews, M. Schmidt, B. T. Soifer, and J. Bennett, Continuum energy distributions of quasars in the Palomar-Green survey, Astrophys. J. **63**, 615 (1987), https://ui.adsabs.harvard.edu/abs/1987ApJS..63..615N/abstract.

[89] A. Baskin and A. Laor, What controls the C IV line profile in active galactic nuclei?, Mon. Not. R. Astron. Soc. **356**, 1029 (2005).

[90] J. E. Scott, G. A. Kriss, M. Brotherton, R. F. Green, J. Hutchings, J. M. Shull, and W. Zheng, A Composite extreme ultraviolet QSO spectrum from FUSE, Astrophys. J. **615**, 135 (2004).

[91] W. N. Brandt, A. Laor, and B. J. Wills, On the nature of soft x-ray weak quasistellar objects, Astrophys. J. **528**, 637 (2000).

[92] S. Wu, Y. Lu, F. Zhang, and Y. Lu, Radiative efficiency of disk accretion in individual SDSS QSOs, Mon. Not. R. Astron. Soc. **436**, 3271 (2013).

[93] I. Banerjee, S. Chakraborty, and S. SenGupta, Excavating black hole continuum spectrum: Possible signatures of scalar hairs and of higher dimensions, Phys. Rev. D **96**, 084035 (2017).

[94] M. Y. Piotrovich, Y. N. Gnedin, T. M. Natsvlishvili, and S. D. Buliga, Constraints on spin of a supermassive black hole in quasars with big blue bump, Astrophys. Space Sci. **362**, 231 (2017).

[95] J. Nash and J. Sutcliffe, River flow forecasting through conceptual models. part I—A discussion of principles, J. Hydrol. **10**, 282 (1970).

[96] D. R. Legates and G. J. McCabe, Evaluating the use of goodness-of-fit measures in hydrologic and hydroclimatic model validation, Water Resour. Res. **35**, 233 (1999).

[97] P. Krause, D. P. Boyle, and F. Bäse, Comparison of different efficiency criteria for hydrological model assessment, Adv. Geosci. **5**, 89 (2005).

[98] C. J. Willmott, On the evaluation of model performance in physical geography, in *Spatial Statistics and Models* (Springer, New York, 1984), pp. 443–460.

[99] C. J. Willmott, On the validation of models, Phys. Geograph. **2**, 184 (1981).